

Dynamically Reconfigurable Optical Skyrmions Enabled by a Silicon Microring Optical Phased Array for Robust Free-Space Communication

Zili Cai, Tian Zhang*, Qi Chen, Zheng Wang, Jian Dai and Kun Xu

*Corresponding author: ztian@bupt.edu.cn

Abstract—Optical skyrmions offer a robust vectorial information degree of freedom for free-space communication, but practical deployment requires a compact platform capable of active topological reconfiguration. Here, we propose a silicon microring-resonator optical phased array that integrates spin-selective emission and programmable phase control on a single chip. Optimized inner- and outer-grating microring emitters provide decoupled LCP and RCP radiation bases with polarization fractions of 90.27% and 91.40%, enabling active switching between Néel-type and Bloch-type skyrmions, while dynamically tuning the skyrmion number across $N_{sk} = -1.914$ to 1.918. Using these programmable topological states, a 4-symbol free-space communication link is constructed and compared with ideal LG-OAM encoding under Kolmogorov turbulence. The skyrmion-encoded link maintains a lower symbol error rate over a broader turbulence range, demonstrating that topological observables are more robust than scalar OAM modes. These results establish actively reconfigurable optical skyrmions as compact, programmable, and turbulence-tolerant information carriers for next-generation free-space optical communication.

Index Terms—Optical skyrmions, Topological photonics, Optical phased arrays, Free-space optical communication, Orbital angular momentum

I. INTRODUCTION

DRIVEN by the rapid development of data-intensive applications such as artificial intelligence and cloud computing, next-generation high-capacity optical communication systems require higher data transmission rates and stronger robustness against channel disturbances [1, 2]. Traditional multiplexing technologies, however, are gradually approaching their physical limits [3-5]. Structured light carrying orbital angular momentum (OAM) has emerged as a promising approach, yet scalar OAM beams are sensitive to phase distortion and turbulence [6-9]. In recent years, optical skyrmions have received widespread attention as a new type of information carrier [10-13]. As a unique two-dimensional vectorial light field, an optical skyrmion exhibits a continuous

and non-trivial wrapping of polarization states across its beam cross-section [10, 14]. More importantly, this topological polarization texture can be generated through the coherent superposition of light fields with orthogonal polarization states and different OAMs, and its topology is characterized by the skyrmion number [14-16]. This physical property has inspired important applications in many fields, including optical manipulation, high-precision sensing, robust information transmission and adaptive photonic devices [10, 11, 17-19].

Although optical skyrmions exhibit broad application prospects, efficiently generating these complex optical fields in practical systems remains a challenge. Currently, the most common approaches to achieve optical skyrmions rely on conventional free-space optical systems. Specifically, researchers typically utilize spatial light modulators (SLMs) [20-22] and q-plates [23, 24] to generate optical skyrmion. However, these systems share intrinsic limitations: their large spatial footprints and highly demanding optical alignment severely constrain their application. To overcome these spatial limitations, researchers have turned to compact micro-/nanophotonic structures such as optical metasurfaces [25, 26]. These structures can precisely manipulate optical fields at the subwavelength scale, enabling compact control of skyrmionic topology and propagation dynamics. Nevertheless, their topological responses are mainly encoded by predesigned passive nanostructures, and therefore they still lack active reconfigurability after fabrication.

More recently, experimental programmable skyrmion platforms based on nonlinear $\chi^{(2)}$ microring resonators (MRRs) [27] and plasmonic [28] have demonstrated dynamic control of topological states. However, their reconfigurability is still limited to a few discrete or binary states, rather than continuous and independent control of skyrmion type and skyrmion number. Recently, a study further demonstrated on-chip optical skyrmion generators based on silicon MRRs [29]. These devices utilize double angular gratings to diffract and superimpose optical beams that possess orthogonal polarization states, thereby successfully generating optical skyrmions on a chip. However, this silicon-MRR scheme remains passive: once the fabrication process is complete, fixed physical structures such as etched grating periods permanently lock the topological charges of the generated beams at a given operating wavelength. This fixed hardware prevents independent control over orthogonal polarization

This work was supported by the National Natural Science Foundation of China (62171055, 62135009, 62471062); Fundamental Research Funds for the Central Universities (ZDYY202102); and the Super Computing Platform of Beijing University of Posts and Telecommunications. (Corresponding author: Tian Zhang.)

Z. Cai, T. Zhang, Q. Chen, Z. Wang, J. Dai, and K. Xu are with the IPOC Laboratory, Beijing University of Posts and Telecommunications, Beijing 100876, China.

components, forcing researchers to fabricate new devices with different structural parameters to switch the output skyrmion states. Consequently, existing integrated skyrmion generators still lack the active and broad topological reconfigurability required for adaptive free-space optical communications.

To overcome the static and limited reconfigurability of existing integrated skyrmion generators, we propose an active generation platform based on a polarization-decoupled silicon MRR optical phased array (OPA). First, the inner-grating MRR (IG-MRR) and outer-grating MRR (OG-MRR) emitters are optimized using evolutionary algorithms to provide decoupled circularly polarized radiation bases. Then, programmable phase-tuning elements are introduced to independently control the phase distributions of the orthogonal polarization components. In this way, the fixed-topology constraint imposed by passive structures is relaxed, and the emitted spin-orbit composition can be actively programmed

on a single chip. Through rigorous numerical simulations, we show that the proposed OPA can dynamically switch between different optical-skyrmion textures and tune the skyrmion number by adjusting the phases of the array elements in real time. Furthermore, we evaluate the propagation of these programmable topological states under atmospheric turbulence and construct a skyrmion-encoded free-space optical communication link. The results show that the extracted skyrmion number remains more robust than scalar OAM modes under turbulence-induced distortions, providing a compact and actively reconfigurable route toward turbulence-tolerant free-space optical communications.

II. DEVICE DESIGN AND THEORETICAL MODEL

A. Configuration of system

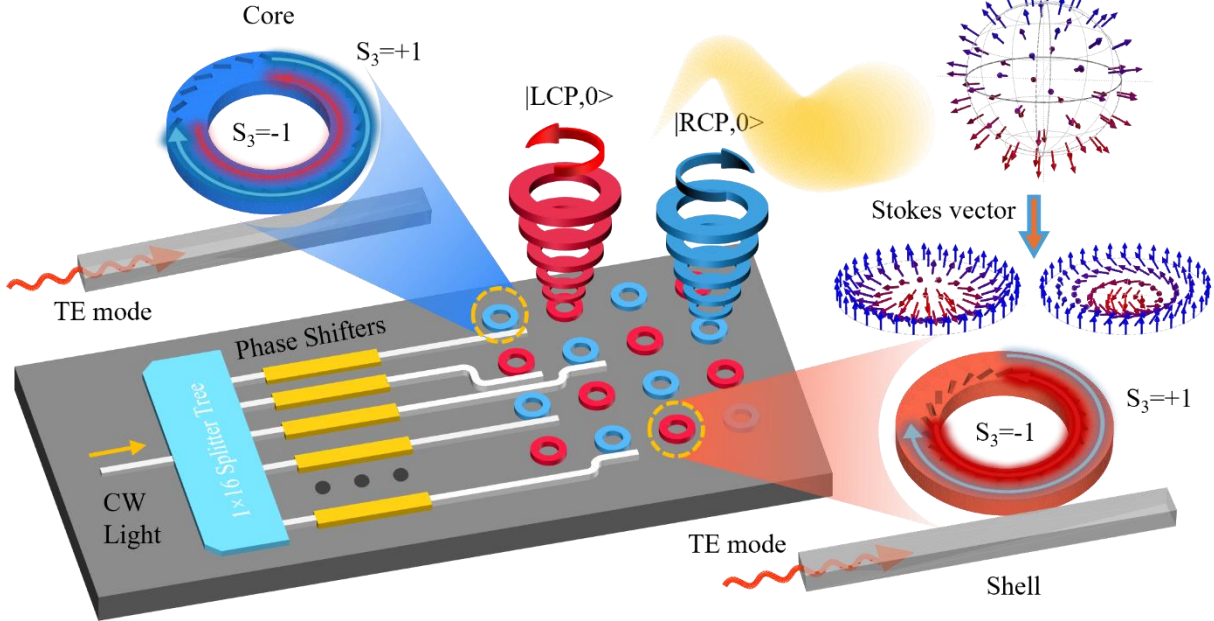


Fig.1 Schematic of the on-chip dynamically reconfigurable optical skyrmion generator. The integrated platform uses a silicon OPA to address a two-dimensional checkerboard array of chiral MRRs. The insets illustrate the decoupled vertical emission of circularly polarized light from the MRRs with inner and outer gratings. The right panel displays the synthesis of the far-field vectorial polarization texture and its geometric mapping onto the Poincaré sphere.

The proposed optical skyrmion generator is based on a silicon chiral optical phased array (OPA), as is shown in Fig. 1. The device is designed on a silicon photonic platform and operates at the telecommunication wavelength of $\lambda_0=1550\text{nm}$. Each emitting element is a silicon MRR placed on a SiO_2 substrate. The ring waveguide has a width of $W_{\text{wg}}=450\text{nm}$ and a height of $H_{\text{wg}}=340\text{nm}$. A straight bus waveguide is placed near each MRR with a coupling gap of 100nm . Therefore, the resonance quality factor discussed in the following section corresponds to the loaded Q of the bus-coupled emitting resonator, rather than the intrinsic Q of an isolated ring.

The OPA maps an in-plane continuous-wave (CW) input light into a free-space vectorial polarization texture. The routing process starts from a designed power distribution network. An injected transverse-electric (TE) mode first

passes through a cascaded 1×16 Y-branch splitter tree, which distributes the input power into multiple waveguide channels with prescribed amplitude weights. Thermo-optic phase shifters integrated on these routing waveguides then independently impose programmable phase delays on the guided TE modes. This modulation network provides amplitude weighting and dynamic phase control for the emitted field, which forms the basis for reconfiguring the topological texture of the optical skyrmion.

The phase-modulated signals then couple into an OPA, which configured as a checkerboard interleaved array of chiral MRRs. Each emitter supports a quasi-TE whispering gallery mode (WGM) near $\lambda_0=1550\text{nm}$. To generate orthogonal polarization states, this emission interface strategically incorporates two distinct structures: IG-MRRs and OG-MRRs.

With a specific optimization strategy, the IG-MRRs emit left-circularly polarized (LCP) light, while the OG-MRRs emit right-circularly polarized (RCP) light. The grating number and MRR radius are designed separately. The grating number controls the OAM order of the dominant circular polarization component, while the MRR radius is adjusted to align the resonance wavelength to 1550nm. The performance of optical skyrmion synthesis depends on the purity of these two circularly polarized light. In the optimization process in section 2.2, we demonstrate two different MRR optimization results. Through high degree of freedom grating optimization, the degree of circular polarization (DOCP) is over 90% for both IG-MRR and OG-MRR.

The quality of skyrmion synthesis depends on the polarization purity, phase accuracy and relative OAM order of these two circularly polarized components [30]. To enable dynamic texture control, the IG-MRRs and OG-MRRs are assigned to different functional groups, referred to as the core group and the shell group, respectively. For each group, a helical wavefront phase and a uniform phase bias are applied through the modulation network. This design allows the OPA to quantitatively control the spin-orbit composition of the emitted vectorial field and enables dynamic reconfiguration of the optical skyrmion texture on chip.

B. Optimization process of IG-MRRs and OG-MRRs

The chiral grating geometry of each MRR emitter is optimized by a particle swarm optimization (PSO) workflow, as shown in Fig.2 (a). The propose of this optimization is to obtain high-purity circularly polarized emission while keeping the grating perturbation compatible with the loaded resonance of the full bus-coupled MRR.

1. Initialization of the optimization parameters. The optimization starts from a three-period local model of the chiral grating section in the MRR. Each particle in the swarm is described by a set of geometric parameters, including the etch depth (d_g), etch length (l_g), etch width (w_g), offset (o_g) and grating tilt angle (θ_g). For a WGM with azimuthal order m and angular grating number g , the grating first defines a structural azimuthal order [31]:

$$l_0 = m - g \quad (1)$$

A radially polarized OAM field with this azimuthal order can be decomposed into two circular polarization components with shifted OAM orders [32]:

$$\hat{\rho}e^{il_0\varphi} \propto \hat{e}_{RCP}e^{i(l_0-1)\varphi} + \hat{e}_{LCP}e^{i(l_0+1)\varphi} \quad (2)$$

where $\hat{\rho}$ is the radial unit vector in cylindrical coordinates, l_0 is the structural azimuthal order defined by the difference between the grating number and the WGM order. \hat{e}_{RCP} and \hat{e}_{LCP} are the unit polarization vectors of the RCP and LCP light. This decomposition shows that the RCP and LCP components carry OAM orders of l_0-1 and l_0+1 , respectively. Here, we set $g=34$ and $m=33$ and the RCP component then carry $l_{RCP}=0$ ($|RCP, l=0\rangle$).

In the PSO initialization, 12 particles are randomly distributed in the predefined geometry bounds. The

ranges are $l_g=60-350\text{nm}$, $w_g=40-130\text{nm}$, $d_g=30-100\text{nm}$, $o_g=0-180\text{nm}$, $\theta_g=-75^\circ-75^\circ$. The initial velocity of each particle is set to zero and the swarm evolved for 25 generations.

2. Set figure of merit (FOM). The FOM is set by considering the polarization purity, upward emission efficiency and back-reflection. The efficiency scale is estimated from the loaded Q of the MRR. Since previous angular-grating silicon MRR emitters had illustrated that $Q=1000-5000$ [29], we select $Q_L=1200$ to favor stronger free-space extraction while preserving resonant operation. For $R=3.2\mu\text{m}$, $\lambda_0=1550\text{nm}$ and an estimated TE group index of $n_g \approx 4.3$, the loaded round-trip loss scale is:

$$\delta_{rt} = \frac{4\pi^2 R n_g}{\lambda_0 Q_L} \approx 29.2\% \quad (3)$$

The δ_{rt} includes bus-waveguide coupling, grating radiation, reflection and other loss channels. The MRR contains 34 gratings while the local model contains three grating periods. The corresponding local perturbation scale is:

$$\delta_{3\text{period}} = \frac{3}{34} \delta_{rt} \approx 2.58\% \quad (4)$$

The upward emission monitored in the local FDTD model is only one useful part of this total loss scale. We therefore set the upper scale of the monitored three-period upward emission to half of this local perturbation scale:

$$\eta_{up} \leq \frac{1}{2} \delta_{3\text{period}} \approx 1.3\% \quad (5)$$

Thus, the target range for the local upward emission is approximately 0-1.3%. In the numerical implementation, a flat-top window is used to keep the grating in a weak-to-moderate perturbation regime. The FOM is then defined as:

$$\begin{aligned} FOM &= I_{pol} |DOCP|^8 P_\eta(\eta_{up}) \exp(-50R_{back}) \\ &= I_{pol} \left| \frac{P_{LCP} - P_{RCP}}{P_{tot}} \right|^8 P_\eta(\eta_{up}) \exp(-50R_{back}) \end{aligned} \quad (6)$$

Here, I_{pol} is a selector parameter. For the RCP target, $I_{pol}=1$ only when $DOCP < 0$; for the LCP target, $I_{pol}=1$ only when $DOCP > 0$. Otherwise, $I_{pol}=0$. The term $|DOCP|^8$ offer high priority to circular polarization purity, while $\exp(-50R_{back})$ penalizes back-reflection. The efficiency term P_η is a flat-top penalty, no penalty is applied when the emit efficiency below $\eta_{up}=1.3\%$. Outside this range, P_η decreases with a Gaussian penalty. P

3. 3 period FDTD simulation. Each particle is evaluated by a three-period 3D-FDTD simulation. A fundamental TE mode is injected into the curved waveguide section. The etched grating scatters part of the guided field into free space. The upward emission is collected by the z-normal field monitor above the grating. The backward power is measured by the reflection monitor and the

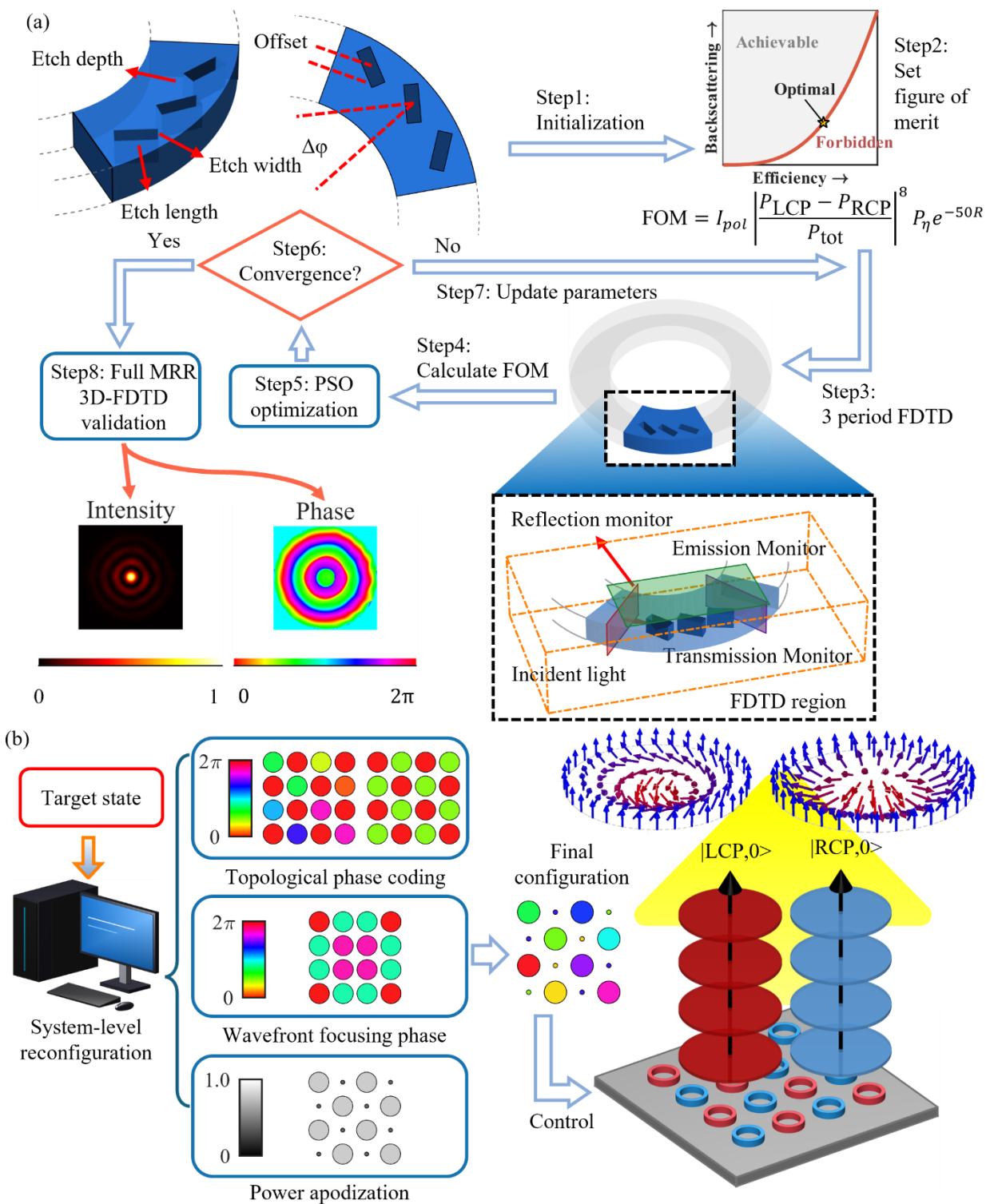


Fig.2 Device-level optimization and array-level synthesis workflow for the proposed OPA skyrmion generator. (a) Device-level optimization of the chiral MRR emitters. The grating geometry is optimized by particle swarm optimization using a three-period FDTD model, where the figure of merit considers circular polarization purity, upward emission efficiency, and back-reflection. The optimized parameters are then validated in the full bus-coupled MRR model through resonant far-field simulations. (b) Array-level synthesis of optical skyrmions. The optimized IG-MRR and OG-MRR emitters form two circularly polarized radiation bases. Programmable OPA phase maps and amplitude weights are applied to the checkerboard emitter array to control the spin-orbit composition and generate reconfigurable skyrmion states.

remaining guided field is tracked by the transmission monitor. This local model keeps the main scattering physics while reducing the cost of repeated full-ring simulations.

4. Calculate FOM. After each FDTD run, the upward field is projected into the far field and decomposed into LCP and RCP components:

$$E_{LCP} = \frac{E_x - iE_y}{\sqrt{2}}, E_{RCP} = \frac{E_x + iE_y}{\sqrt{2}} \quad (7)$$

$$P_{LCP} = |E_{LCP}|^2, P_{RCP} = |E_{RCP}|^2 \quad (8)$$

5. PSO optimization. The PSO optimization is performed using the FOM obtained from the three-period FDTD model. For each particle, a candidate grating geometry is constructed and simulated.
6. Check for convergence. After each generation, the algorithm checks whether the optimization has converged. If the best global FOM becomes stable or the maximum generation number (here is 25) is reached, the optimization proceeds to step 8. Otherwise, the workflow returns to step 7.
7. Update parameters. If convergence conditions are not satisfied, the particle parameters are updated within the predefined bounds. The etch length, etch width, etch depth, radial offset, and tilt angle are renewed for the next generation. Then repeat step 3 to step 6.
8. Full MRR 3D-FDTD validation. After convergence, the best local grating geometry is transferred to the complete MRR for 3D-FDTD validation. The full model includes the complete angular grating array and the bus-waveguide coupling. This simulation verifies the loaded resonance, resonant emission efficiency, farfield intensity and phase distribution. For the representative OG-MRR, the optimized geometry is $l_g=350\text{nm}$, $w_g=78.7\text{nm}$, $d_g=81.3\text{nm}$, $o_g=115.9\text{nm}$, $\theta_g=-33.7^\circ$. The optimized three-period unit gives an upward emission efficiency of 0.46%, a DOCP of -0.82, a reflection of 0.83% and a final FOM of 0.14.

C. Far-field Skyrmion Evolution and Topological Invariants

The optimized IG-MRR and OG-MRR emitters provide two circularly polarized radiation bases for the OPA. As shown in Fig. 2(b), the array-level synthesis includes power distribution optimization and phase programming. The power distribution controls the amplitude balance between the two spin channels. The phase programming controls the OAM order, the relative phase, and the focusing wavefront of the emitted field.

For the j -th emitter located at the transverse coordinate $\mathbf{r}_j=(x_j, y_j)$, its azimuthal position is defined as $\varphi_j=\text{atan2}(y_j, x_j)$. The complex excitation coefficient in the σ -polarized channel is $c_j^\sigma = a_j^\sigma \exp(i\Phi_j^\sigma)$, where $\sigma \in \{RCP, LCP\}$. The parameter a_j^σ is the amplitude weight and Φ_j^σ is the programmed phase delay. The amplitude weights are set by the splitter network. They are optimized to compensate for the different radiation efficiencies, propagation losses, and spatial overlaps of the two subarrays. This step helps the RCP and LCP components reach comparable amplitudes in the target region of interest. Such amplitude balance is needed for a clear polarization

wrapping on the Poincaré sphere. The phase delay applied to each emitter is written as:

$$\Phi_j^\sigma = l_{OPA}^\sigma \varphi_j + \delta_\sigma + \Phi_{foc,j} \quad (9)$$

here, l_{OPA}^σ is the programmable OAM order imposed by the OPA phase gradient on the σ -polarized subarray, $l_{OPA}^\sigma \varphi_j$ forms a helical phase distribution across the array. δ_σ is a uniform phase bias applied to the entire σ -polarized subarray. $\Phi_{foc,j}$ is the wavefront focusing phase of the j -th emitter. This phase term is used to focus the emitted field onto the selected observation plane. It also helps improve the energy concentration and the spatial overlap of the two spin components within the ROI. For a target focal point $\mathbf{r}_f=(x_f, y_f, z_f)$, the focusing phase can be written as:

$$\Phi_{foc,j} = -k_0(|\mathbf{r}_f - \mathbf{r}_j| - |\mathbf{r}_f|) \quad (10)$$

Where $k_0=2\pi/\lambda$ is the free-space wavenumber and λ is the operating wavelength. The vector \mathbf{r}_f gives the target focal position. Each chiral MRR also provides an intrinsic OAM order l_{MRR}^σ , which is set by its angular grating structure. The total OAM order in the far field is:

$$l_{tot}^\sigma = l_{MRR}^\sigma + l_{OPA}^\sigma \quad (11)$$

This relation shows that the MRR provides a fixed spin-OAM basis, while the OPA adds a programmable OAM order. Therefore, the device can change the emitted spin-orbit state without changing the fabricated grating geometry. The synthesized far-field vector beam can be described as:

$$\mathbf{E}(\rho, \phi) = A_R(\rho) e^{il_{tot}^R \phi + i\delta_R} |R\rangle + A_L(\rho) e^{il_{tot}^L \phi + i\delta_L} |L\rangle \quad (12)$$

where (ρ, ϕ) are the polar coordinates in the observation plane. $A_R(\rho)$ and $A_L(\rho)$ are the radial amplitude envelopes of the RCP and LCP components. The vectors $|R\rangle$ and $|L\rangle$ are the unit polarization vectors of the two circular polarization states. These radial envelopes are affected by the MRR radiation pattern, the OPA array factor, the amplitude weights a_j^σ , and the focusing phase $\Phi_{foc,j}$. When the two spin components carry different total OAM orders, their coherent superposition forms a spatially varying polarization texture.

The skyrmion number is mainly controlled by the OAM difference between the two spin components. We define this difference as $\Delta l = l_{tot}^L - l_{tot}^R$. Here, Δl describes the relative phase winding between the LCP and RCP components. By tuning l_{OPA}^R and l_{OPA}^L , the OPA changes Δl , and thus programs the skyrmion number. In the balanced case, the designed skyrmion number approximately follows $N_{sk} \approx \Delta l$.

The skyrmion type is controlled by the relative phase bias between the two spin channels. We define this bias as $\Delta \delta = \delta_L - \delta_R$. This parameter does not change Δl , so it does not change the skyrmion number. Instead, it rotates the in-plane polarization texture. The local polarization orientation angle can be written as:

$$\psi(\rho, \phi) = \frac{1}{2}(\Delta l \phi + \Delta \delta) \quad (13)$$

where $\psi(\rho, \phi)$ is the orientation angle of the local polarization ellipse. This relation indicates that Δl sets the

winding rate of the texture, while $\Delta\delta$ sets its overall rotation. A radial polarization texture corresponds to a Néel-type optical skyrmion, and an azimuthal polarization texture corresponds to a Bloch-type optical skyrmion. Intermediate values of $\Delta\delta$ generate hybrid textures.

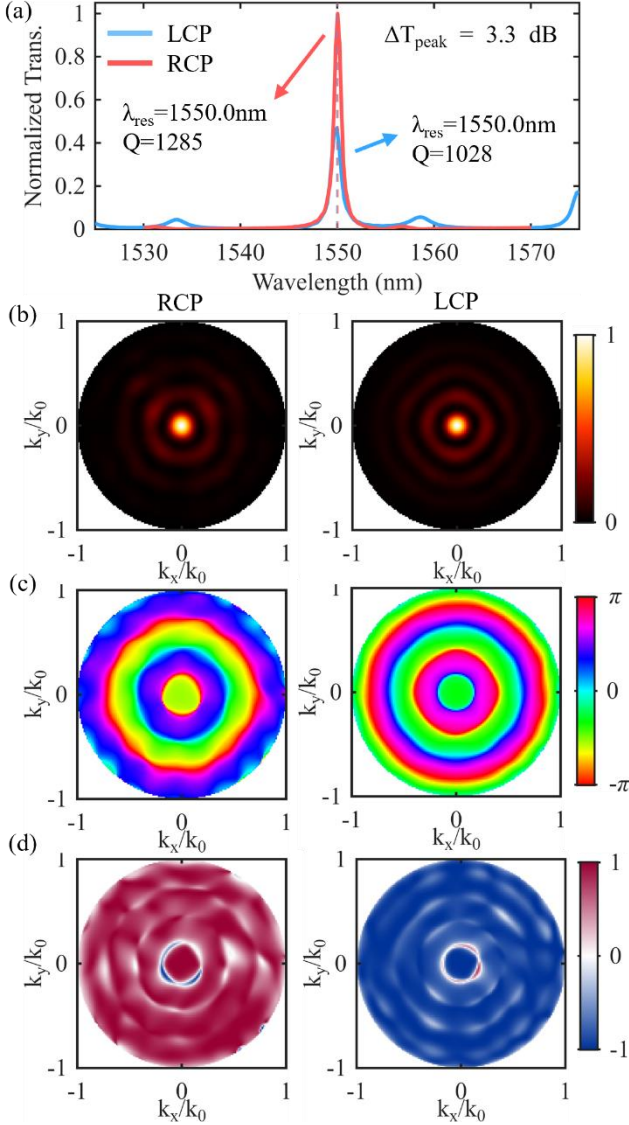


Fig.3 (a) Normalized transmission spectra of the optimized IG-MRR and OG-MRR. Both emitters resonate at $\lambda_{\text{res}}=1550.0\text{nm}$, with loaded quality factors of $Q=1028$ and $Q=1285$, respectively. The peak transmission difference is $\Delta T_{\text{peak}}=3.3\text{dB}$. (b) Far-field intensity profiles of the two emitters in the $(k_x/k_0, k_y/k_0)$ plane. (c) Far-field phase distributions. Both emitters show radial phase rings without spiral phase winding, indicating 0 intrinsic topological charge. (d) Far-field degree of circular polarization distributions. The LCP emitter shows a DOCP of 0.8056, an LCP fraction of 90.27% and a peak upward efficiency of 1.43%. The RCP emitter shows a DOCP of -0.8279, an RCP fraction of 91.40% and a peak upward efficiency of 3.04%.

To evaluate the topology of the generated field, the local polarization state is mapped to the normalized Stokes vector $\mathbf{n}(x, y) = [S_1(x, y), S_2(x, y), S_3(x, y)] / S_0(x, y)$. Here, S_0 is the total intensity. S_1 and S_2 describe the linear polarization

components and S_3 describes the circular polarization component. The skyrmion number is defined as:

$$N_{sk} = \frac{1}{4} \iint_{\Omega} \mathbf{n} \cdot \left(\frac{\partial \mathbf{n}}{\partial x} \times \frac{\partial \mathbf{n}}{\partial y} \right) dx dy \quad (14)$$

Here, Ω is the region of interest for the topological evaluation. In this work, Ω is selected as the central main-lobe region bounded by the first radial intensity minimum. This choice reduces the influence of radial side lobes, which may carry alternating skyrmion and anti-skyrmion contributions. It also gives a clear region for defining the encoded topological state in free-space optical communication.

III. RESULTS

A. MRRs

Fig. 3 shows the full-ring FDTD validation of the optimized chiral MRR emitters. The optimized grating parameters are first obtained from the local three-period model and are then transferred to the complete bus-coupled MRR. This full-ring simulation checks whether the optimized emitters can still provide resonant emission, spin-selective radiation, and topologically neutral phase bases in the complete device.

The transmission spectra in Fig. 3(a) shows that both emitters resonate at $\lambda_{\text{res}}=1550.0\text{nm}$, which matches the target wavelength. The loaded quality factors are $Q=1028$ for the LCP emitter and for the $Q=1285$ RCP emitter. These values indicate that the optimized gratings introduce useful radiation loss while keeping clear resonances. The peak transmission difference is $\Delta T_{\text{peak}}=3.3\text{dB}$, which suggests that the two spin channels need power balancing in the later OPA synthesis.

In the far field, the two emitters produce similar intensity profiles in the $(k_x/k_0, k_y/k_0)$ plane, as shown in Fig. 3(b). Both profiles contain a central main lobe and weak radial side lobes. This spatial similarity provides compatible radiation bases for coherent superposition. The phase distributions in Fig. 3(c) further show radial phase rings rather than spiral phase winding. This feature indicates that the intrinsic topological charges of the two emitters are zero. Therefore, the optimized MRRs provide topologically neutral spin bases, while the required OAM orders are introduced later by the programmable phase gradients of the OPA.

The circular polarization maps in Fig. 3(d) show opposite DOCP signs for the two emitters over most of the radiation region. The LCP emitter (IG-MRRs) has a DOCP of 0.8054, an LCP fraction of 90.26% and a peak upward efficiency of 1.43%. The RCP emitter (OG-MRRs) has a DOCP of -0.8279, an RCP fraction of 91.40% and a peak upward efficiency of 3.04%. These values confirm that the optimized chiral gratings generate two separated spin channels with high polarization selectivity. The efficiency difference also supports the need for array-level power balancing before coherent OPA synthesis.

These device-level results establish the emitter basis for the following OPA synthesis. The optimized IG-MRR and OG-MRR operate at the target wavelength, provide compatible far-field intensity profiles, maintain zero intrinsic topological

charge, and generate opposite circular polarization states.

B. Phase-Controlled Skyrmion Type Switching

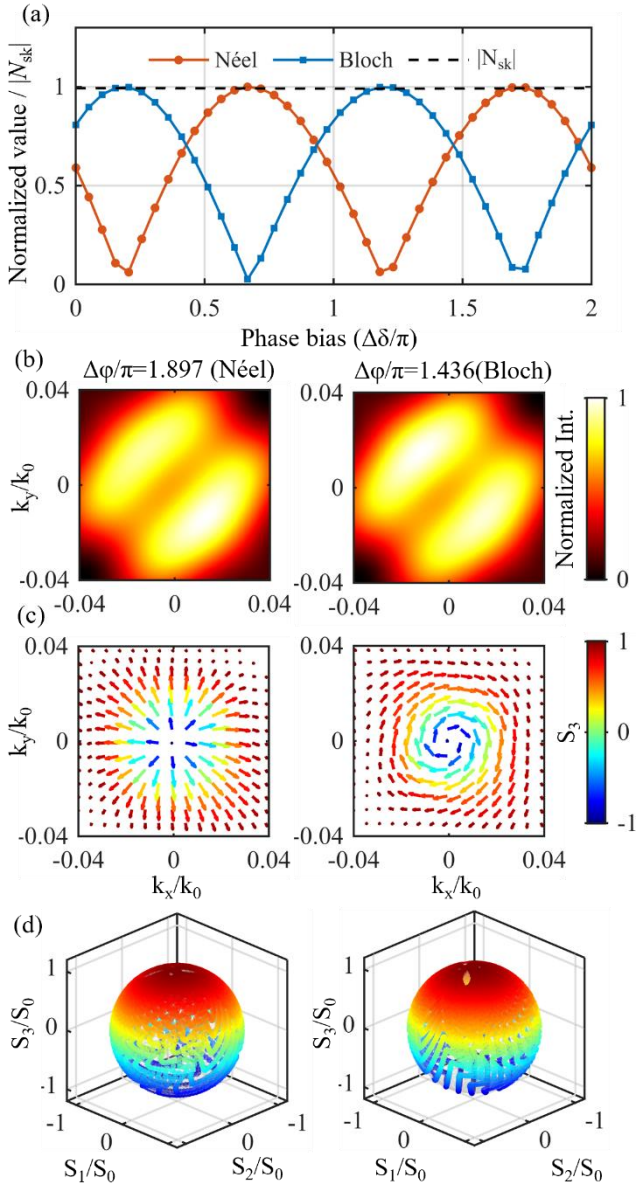


Fig.4 (a) Phase-controlled conversion between Néel-type and Bloch-type optical skyrmions as a function of the relative bias $\Delta\delta/\pi$. The red and blue solid curves show the normalized Néel-like and Bloch-like components, respectively. These components are obtained by projecting the local in-plane polarization vectors onto the radial and azimuthal directions. The black dashed line shows $|N_{sk}|$. The selected Néel-type state occurs at $\Delta\delta=1.436\pi$, with a Néel-like component of 0.998 and $|N_{sk}|=0.988$. The selected Bloch-type state occurs at $\Delta\delta=1.897\pi$, with a Bloch-like component of 1.000 and $|N_{sk}|=0.988$. (b) Normalized far-field intensity distributions of the selected Néel-type and Bloch-type states in the observation region. (c) Local polarization maps of the selected states. The arrows indicate the in-plane polarization orientation, and the color represents the out-of-plane Stokes component S_3 . (d) Mapping of the normalized Stokes vector $\mathbf{n}=(S_1,S_2,S_3)/S_0$ onto the Poincaré sphere for the two skyrmion types.

After the device-level validation, we further examine the

type tunability of the optical skyrmion generated by the interleaved OPA. In this test, the OAM difference $\Delta l = l_{tot}^L - l_{tot}^R$ is kept unchanged, while only the relative phase bias $\Delta\delta = \delta_L - \delta_R$ is varied. This setting separates the control of skyrmion type from the control of skyrmion number. It also tests the design rule that $\Delta\delta$ rotates the in-plane polarization texture, whereas Δl determines the topological order.

The phase-dependent evolution in Fig. 4(a) confirms this control mechanism. The Néel-like component describes the radial part of the in-plane polarization texture, and the Bloch-like component describes the azimuthal part. As $\Delta\delta$ changes, these two components exchange their dominant roles in a periodic way. This behavior shows that the relative phase bias mainly rotates the local polarization orientation within a similar optical field envelope. When the radial component is dominant, the synthesized field approaches a Néel-type skyrmion. When the azimuthal component is dominant, the field approaches a Bloch-type skyrmion. This periodic exchange indicates that the OPA can continuously tune the texture type through phase control, rather than by changing the device geometry.

The nearly unchanged $|N_{sk}|$ in Fig. 4(a) gives the key evidence for independent type control. The selected Néel-type state has a Néel-like component of 0.998 at $\Delta\delta=1.436\pi$ with $|N_{sk}|=0.988$. The selected Bloch-type state has a Bloch-like component of 1.000 at $\Delta\delta=1.897\pi$ with $|N_{sk}|=0.988$. These values show that the phase bias changes the texture morphology, but it does not change the topological order. This result agrees with the relation in $\psi(\rho, \phi) = \frac{1}{2}(\Delta l \phi + \Delta \delta)$

discussed in section II, where $\Delta\delta$ gives a global rotation of the local polarization angle.

The representative field maps in Fig. 4(b) and Fig. 4(c) provide a more direct view of this type conversion. The normalized intensity distributions of the selected Néel-type and Bloch-type states in Fig. 4(b) remain similar in the observation region. This similarity indicates that the switching is not caused by a large change in the intensity envelope. Instead, the difference mainly appears in the local polarization direction. As shown in Fig. 4(c), in the Néel-type state, the in-plane polarization vectors mainly point along the radial direction. In the Bloch-type state, these vectors mainly follow the azimuthal direction around the beam center. The S_3 distribution supplies the out-of-plane polarization component, so the field forms a three-dimensional polarization texture rather than a purely transverse vector pattern. Therefore, the field maps connect the phase-controlled rotation in Fig. 4(a) with the real-space polarization morphology.

The Poincaré-sphere mappings in Fig. 4(d) further support this interpretation. Both selected states provide similar coverage of the normalized Stokes vector \mathbf{n} over the sphere. This similar coverage explains why their skyrmion numbers remain almost the same. The main difference between the two states is the orientation of the in-plane texture, not the number of times that \mathbf{n} wraps the sphere. These results show that the

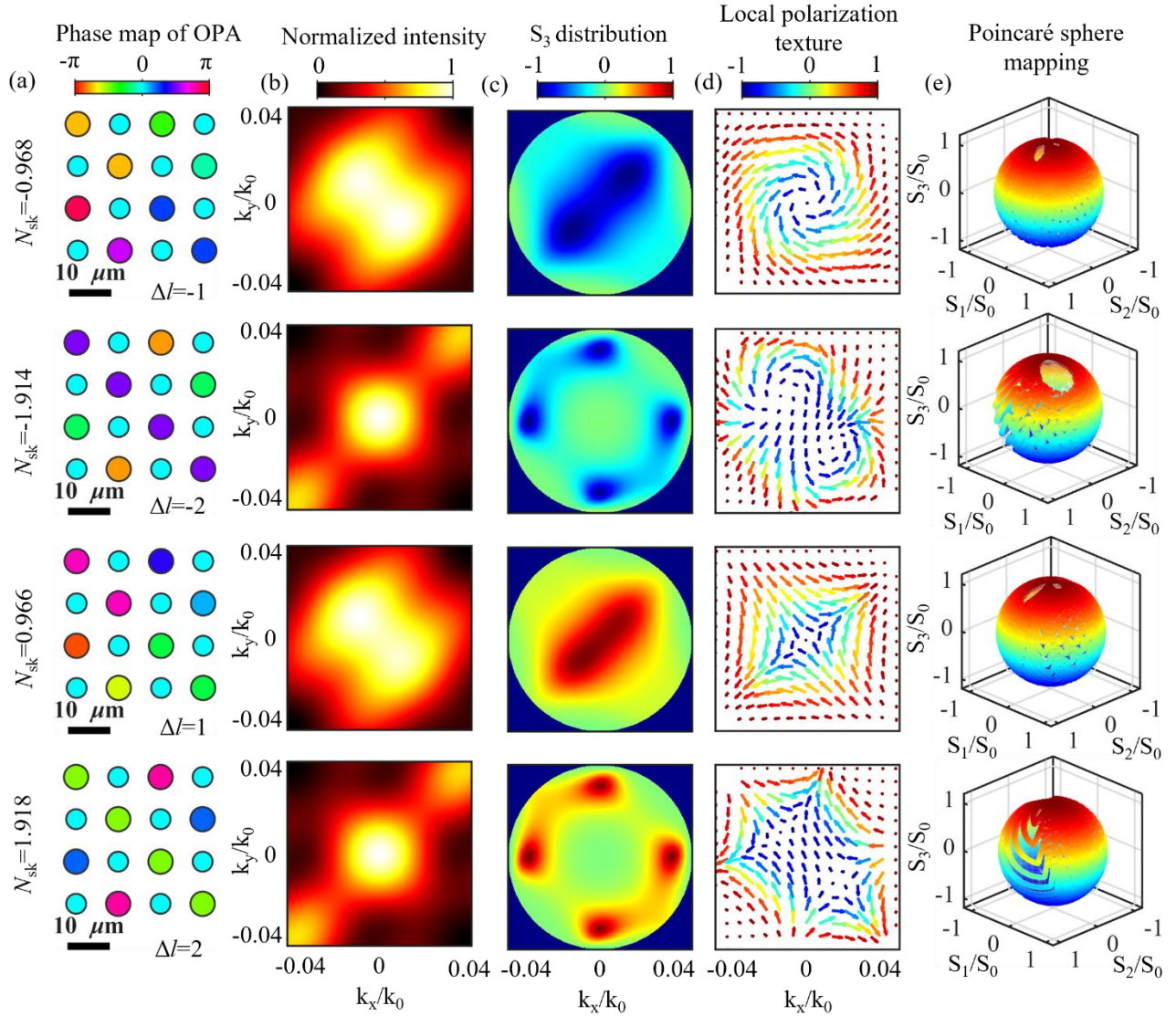


Fig.5 Dynamic reconfiguration of the optical skyrmion number by programmable OPA phase gradients. Each row corresponds to one programmed topological state, while columns show (a) the OPA phase map, (b) the normalized far-field intensity, (c) the out-of-plane Stokes component S_3/S_0 , (d) the local polarization texture, (e) the corresponding Poincaré-sphere mapping of the normalized Stokes vector. From top to bottom, the four states correspond to $\Delta l = -1, -2, 1$ and 2 , with calculated skyrmion numbers of $N_{sk} = -0.968, -1.914, 0.966$ and 1.918 , respectively. In (d), arrows indicate the in-plane polarization orientation and colors represent S_3/S_0 .

proposed OPA can realize phase-only switching between Néel-type and Bloch-type optical skyrmions while preserving the designed topological number. This type tunability provides the first level of array-level reconfigurability before tuning the skyrmion number itself.

C. Dynamic Reconfiguration of Skyrmion Number

After confirming the phase-controlled conversion between Néel-type and Bloch-type textures, we further study the dynamic reconfiguration of the skyrmion number. Here, the relative phase bias $\Delta\delta$ is kept fixed, while the OPA phase gradient is used to change the OAM difference Δl between the LCP and RCP components. In this way, the type control and the number control are separated.

The same optimized emitters and checkerboard OPA geometry are used for all four states. The RCP subarray serves

as the reference channel, while the LCP subarray is assigned an additional azimuthal phase term. This operation changes l_{OPA}^L and therefore tunes $\Delta l = l_{tot}^L - l_{tot}^R$ without modifying the MRR gratings. In the array synthesis, the two spin channels are also power balanced according to their FDTD-calculated far-field energies in the selected ROI, so that a clear polarization wrapping can be formed.

As shown in Fig. 5, the calculated skyrmion number follows the programmed OAM difference. Reversing the sign of Δl reverses the sign of N_{sk} , which indicates that the handedness of the polarization wrapping is controlled by the OPA phase gradient. Increasing Δl leads to a faster in-plane polarization rotation around the beam center and produces a higher-order skyrmion texture. The obtained N_{sk} values remain close to the target integer orders, confirming that Δl is an effective control

parameter for skyrmion-number switching.

The small deviations from ideal integers mainly result from the finite array aperture, residual amplitude mismatch between the two spin channels, non-identical far-field profiles of the unit emitters, and imperfect circular polarization purity. Nevertheless, the overall correspondence between Δl and N_{sk} is well preserved. Together with Fig. 4, these results show that

the proposed OPA can independently control the skyrmion type through $\Delta\delta$ and the skyrmion number through Δl , enabling multiple programmable topological states on a single integrated platform.

IV. SKYRMION-ENCODED FREE-SPACE OPTICAL COMMUNICATION

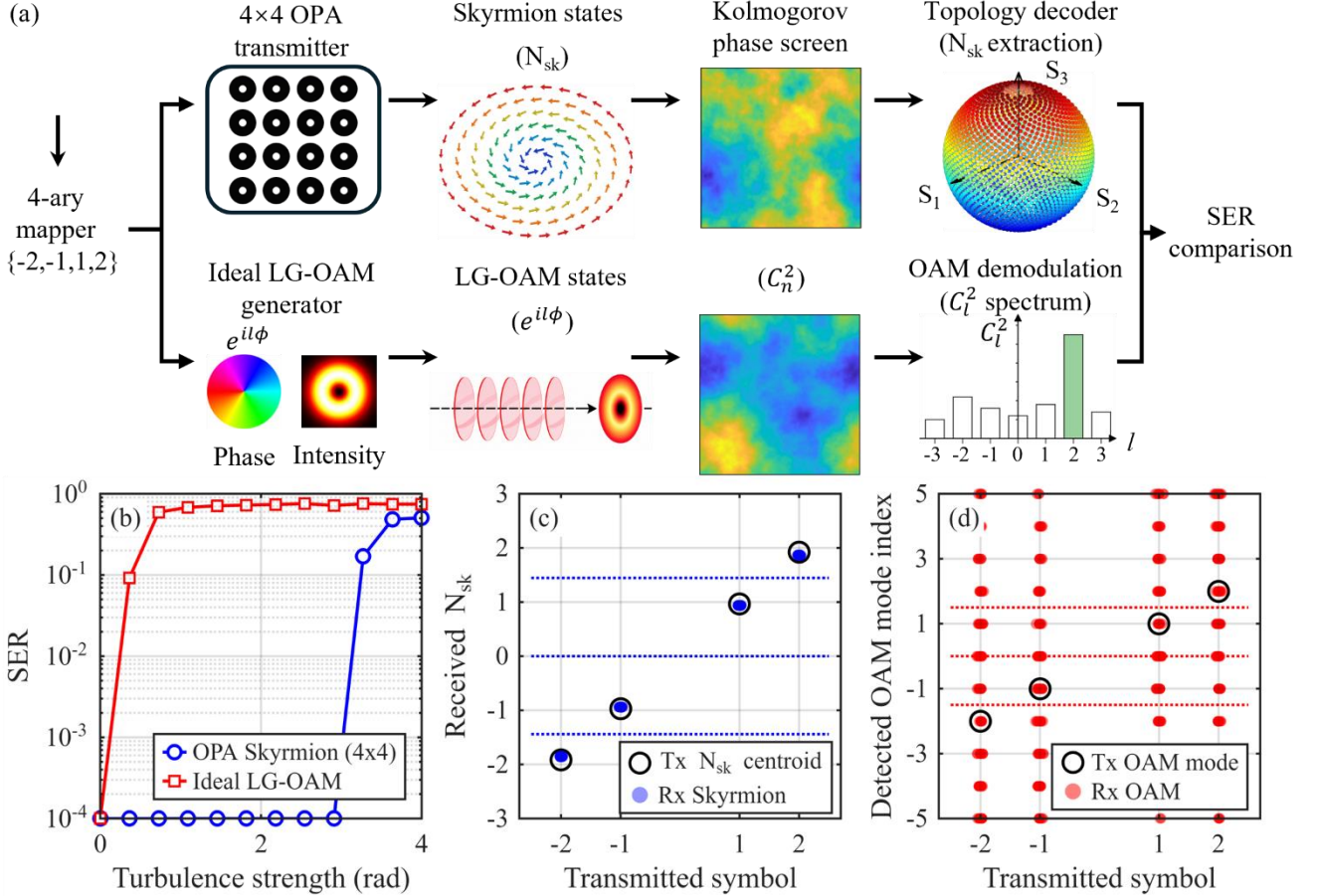


Fig.6 Skyrmion-encoded free-space optical communication under turbulence. (a) Schematic comparison between the proposed OPA-skyrmion link and the ideal LG-OAM link using the same 4-ary symbol set $\{-2, -1, 1, 2\}$. (b) SER versus turbulence strength, obtained from 500 Monte Carlo trials at each turbulence level. (c) Received N_{sk} distribution for the skyrmion link at a turbulence strength of approximately 1.09 rad. (d) Detected OAM mode distribution for the ideal LG-OAM link under the same condition. Black circles indicate transmitted references, and colored points indicate received symbols.

To evaluate the application potential of the reconfigurable skyrmion states, we further construct a 4-ary free-space optical communication link, as shown in Fig. 6(a). The transmitted symbols are selected from $\{-2, -1, 1, 2\}$ and are directly mapped to the programmed OAM difference Δl of the OPA. At the receiver, the skyrmion channel is decoded by extracting the received N_{sk} and comparing it with the calibrated topological centroids obtained from the noiseless transmitter. For comparison, an ideal LG-OAM link with the same symbol set is also simulated, where the receiver detects the dominant OAM mode from the modal spectrum.

The two links are transmitted through the same Kolmogorov phase-screen channel. For each turbulence strength, the SER is obtained from 500 Monte Carlo trials, and the turbulence strength is scanned from weak to strong phase distortion. In the skyrmion link, a weak polarization differential perturbation is

also included to model the relative phase disturbance between the two spin components. This setting allows a direct comparison between topology-based decoding and conventional scalar OAM-mode decoding under the same propagation disturbance.

The SER curves in Fig. 6(b) show that the skyrmion-encoded link has a clear robustness advantage. The OPA-skyrmion channel maintains a low SER over a broad turbulence range, while the ideal LG-OAM channel degrades rapidly as the turbulence strength increases. This result indicates that the extracted N_{sk} is less sensitive to random phase distortion than the scalar OAM mode index. Although the local field profile is disturbed by turbulence, the global polarization wrapping can still remain distinguishable enough for symbol decisions.

The scatter distributions in Fig. 6(c) and Fig. 6(d) further explain this difference. In Fig. 6(c), the received N_{sk} values

remain clustered around their calibrated topological centroids at the selected turbulence strength. Therefore, the nearest-neighbor decoder can still separate the four transmitted symbols. In contrast, Fig. 6(d) shows that the detected OAM mode index spreads over multiple modes under the same turbulence condition. This mode hopping causes stronger symbol ambiguity and leads to a higher SER.

These results show that the programmable skyrmion number is not only a tunable topological property, but also a useful information dimension for free-space optical communication. Compared with ideal LG-OAM encoding, the proposed OPA-skyrmion scheme uses a vectorial topological observable as the decoding feature. This gives the link stronger tolerance to turbulence-induced phase distortions and supports robust multi-symbol transmission on a compact integrated platform.

V. CONCLUSION

We have demonstrated that optical skyrmions can be actively generated and reconfigured on a silicon photonic platform using a microring-resonator optical phased array. The optimized inner- and outer-grating MRR emitters provide decoupled LCP and RCP radiation bases with polarization fractions above 90%, forming a robust foundation for coherent skyrmion synthesis. Independent control of the relative phase bias $\Delta\delta$ and the OAM difference Δl enables switching between Néel-type and Bloch-type textures and dynamic tuning of N_{sk} from -1.914 to 1.918. A 4-symbol free-space communication link demonstrates that the extracted N_{sk} maintains a lower symbol error rate than the scalar OAM mode index under Kolmogorov turbulence, confirming the robustness of topological observables. These results establish actively reconfigurable optical skyrmions as compact, programmable, and turbulence-tolerant carriers for high-dimensional free-space optical communication, bridging integrated photonics with topological structured-light applications.

REFERENCES

- [1] L. Torrijos-Morán and D. Pérez-López, "Industry insight: photonics to scale AI data centers," *npj Nanophotonics*, vol. 3, no. 1, pp. 8, 2026.
- [2] B. Corcoran, A. Mitchell, R. Morandotti, L. K. Oxenløwe, and D. J. Moss, "Optical microcombs for ultrahigh-bandwidth communications," *Nature Photonics*, vol. 19, no. 5, pp. 451-462, 2025.
- [3] X. Zhou, D. Yi, D. W. U. Chan, and H. K. Tsang, "Silicon photonics for high-speed communications and photonic signal processing," *npj Nanophotonics*, vol. 1, no. 1, pp. 27, 2024.
- [4] Z. Zhu *et al.*, "Compensation-free high-dimensional free-space optical communication using turbulence-resilient vector beams," *Nature Communications*, vol. 12, no. 1, pp. 1666, 2021.
- [5] M. Guan *et al.*, "High-performance 100 Gbps free-space optical communication via optical pin beam receiver," *Communications Engineering*, vol. 4, no. 1, pp. 203, 2025.
- [6] J. Wang, J. Liu, S. Li, Y. Zhao, J. Du, and L. Zhu, "Orbital angular momentum and beyond in free-space optical communications," *Nanophotonics*, vol. 11, no. 4, pp. 645-680, 2022.
- [7] A. E. Willner, K. Pang, H. Song, K. Zou, and H. Zhou, "Orbital angular momentum of light for communications," *Applied Physics Reviews*, vol. 8, no. 4, pp. 041312, 2021.
- [8] K. Zou *et al.*, "High-capacity free-space optical communications using wavelength- and mode-division-multiplexing in the mid-infrared region," *Nature Communications*, vol. 13, no. 1, pp. 7662, 2022.
- [9] P. Ju *et al.*, "Atmospheric Turbulence Effects on the Performance of Orbital Angular Momentum Multiplexed Free-Space Optical Links Using Coherent Beam Combining," *Photonics*, vol. 10, no. 6, pp. 634, 2023.
- [10] Y. Shen, Q. Zhang, P. Shi, L. Du, X. Yuan, and A. V. Zayats, "Optical skyrmions and other topological quasiparticles of light," *Nature Photonics*, vol. 18, no. 1, pp. 15-25, 2024.
- [11] A. A. Wang *et al.*, "Topological protection of optical skyrmions through complex media," *Light: Science & Applications*, vol. 13, no. 1, pp. 314, 2024.
- [12] S. Tsesses, E. Ostrovsky, K. Cohen, B. Gjonaj, N. H. Lindner, and G. Bartal, "Optical skyrmion lattice in evanescent electromagnetic fields," *Science*, vol. 361, no. 6406, pp. 993-996, 2018.
- [13] L. Du, A. Yang, A. V. Zayats, and X. Yuan, "Deep-subwavelength features of photonic skyrmions in a confined electromagnetic field with orbital angular momentum," *Nature Physics*, vol. 15, no. 7, pp. 650-654, 2019.
- [14] Z. Ye *et al.*, "Theory of paraxial optical skyrmions," *Proceedings of the Royal Society A: Mathematical, Physical and Engineering Sciences*, vol. 480, no. 2297, 2024.
- [15] W. Lin, Y. Ota, Y. Arakawa, and S. Iwamoto, "Microcavity-based generation of full Poincaré beams with arbitrary skyrmion numbers," *Physical Review Research*, vol. 3, no. 2, pp. 023055, 2021.
- [16] A. McWilliam *et al.*, "Topological Approach of Characterizing Optical Skyrmions and Multi-Skyrmions," *Laser & Photonics Reviews*, vol. 17, no. 9, pp. 2300155, 2023.
- [17] T. He *et al.*, "Optical skyrmions from metafibers with subwavelength features," *Nature Communications*, vol. 15, no. 1, pp. 10141, 2024.
- [18] X. Fan *et al.*, "Topological state and number transitions of optical skyrmions upon free-space beam propagation," *Communications Physics*, vol. 8, no. 1, pp. 500, 2025.
- [19] A. Yang *et al.*, "Spin-Manipulated Photonic Skyrmion-Pair for Pico-Metric Displacement Sensing," *Advanced Science*, vol. 10, no. 12, pp. 2205249, 2023.
- [20] Y. Shen, E. C. Martínez, and C. Rosales-Guzmán, "Generation of Optical Skyrmions with Tunable Topological Textures," *ACS Photonics*, vol. 9, no. 1, pp. 296-303, 2022.

- [21] H. Zhang, C. Gao, and S. Fu, "Selective formation of generalized optical skyrmions," *Optics Letters*, vol. 50, no. 9, pp. 2840-2843, 2025.
- [22] W. Zhen *et al.*, "Reconfiguring optical skyrmion topology in free space," *Optica*, vol. 13, no. 2, pp. 188-194, 2026.
- [23] V. Hakobyan and E. Brasselet, "Q-Plates: From Optical Vortices to Optical Skyrmions," *Physical Review Letters*, vol. 134, no. 8, pp. 083802, 2025.
- [24] J. Geng, S. R. Allam, Q. Sheng, and T. Omatsu, "Generation of Optical Quasiparticles with Spin-Orbit Conversion in a Single Q-Plate," *Laser & Photonics Reviews*, vol. n/a, no. n/a, pp. e02439, 2025.
- [25] N. Mata-Cervera *et al.*, "Tailoring propagation-invariant topology of optical skyrmions with dielectric metasurfaces," *Nanophotonics*, vol. 14, no. 23, pp. 4069-4077, 2025.
- [26] T. He *et al.*, "The longitudinal dynamics evolution of optical skyrmions via meta-optics," *Nanophotonics*, vol. 14, no. 24, pp. 4365-4376, 2025.
- [27] D. Wei *et al.*, "Nanophotonic chip-space interfaces for multidimensional nonlinear optics," *Nature Materials*, 2026.
- [28] L. Chen *et al.*, "Programmable skyrmions for communication and sensing," *Nature Electronics*, 2026.
- [29] W. Lin, Y. Ota, Y. Arakawa, and S. Iwamoto, "On-chip optical skyrmionic beam generators," *Optica*, vol. 11, no. 11, pp. 1588-1594, 2024.
- [30] X. Lei *et al.*, "Photonic Spin Lattices: Symmetry Constraints for Skyrmion and Meron Topologies," *Physical Review Letters*, vol. 127, no. 23, pp. 237403, 2021.
- [31] X. Cai *et al.*, "Integrated Compact Optical Vortex Beam Emitters," *Science*, vol. 338, pp. 363, 2012.
- [32] L. Massai, T. Schatteburg, J. P. Home, and K. K. Mehta, "Pure circularly polarized light emission from waveguide microring resonators," *Applied Physics Letters*, vol. 121, no. 12, pp. 121101, 2022.